Kasetsart J. (Nat. Sci.) 48 : 823 - 835 (2014)

Visualization of Thermal Structure of Turbulent Spot under Adverse Pressure Gradients Using Liquid Crystals

Weerachai Chaiworapuek*, Suttaya Nongnoi and Chawalit Kittichaikarn

ABSTRACT

The pressure gradient affects the stretching and retracting of a streamwise length of the transition zone of a fluid flow over a flat plate. Furthermore, the turbulent spot is directly controlled in size by the pressure gradient. The details were investigated of the evolution of the thermal footprint (the area of heat transfer underneath a turbulent spot) using thermochromic liquid crystals under various adverse pressure gradients. The experiment was carried out over an isothermal flat plate in a low turbulence water tunnel with a turbulent intensity of 0.925%. Information was obtained on the development of the temperature, the heat transfer coefficient and the heat flux contours of the footprint as it propagated downstream. All spot parameters in this study, achieved from the use of the developed image processing code were slightly different to those reported by others. The heat transfer characteristics of the footprint were deduced by an "implicit" heat balance approach. Moreover, the characteristics of the turbulence breaking down under the influence of adverse pressure gradients were presented by representative structures of the turbulent spot footprint. Thus, these results could be applied as qualitative and quantitative data into numerically predictive formulas, used for the flow under a boundary layer transition, induced by an adverse pressure gradient.

Keywords: turbulent spot, adverse pressure gradient, boundary layer transition, liquid crystals

INTRODUCTION

The turbulent spot was first discovered by Emmons (1951) as a small turbulent patch embedded by the laminar flow that grew in both the streamwise and spanwise directions as it propagated downstream. After it merges with neighbors, a fully turbulent boundary layer is formed. Turbulent spots are found at the last state of the boundary layer transition except where the boundary layer is bypassed by suitable disturbance. Following Walker and Gostelow (1998), it was found that the characteristics of an artificially generated spot in bypassed transition were equivalent to those occurring on a compressor stator blade. Schubauer and Klebanoff (1955) first reported that a turbulent spot has an arrowhead shape with a propagation rate of 0.88 and 0.5 at the leading (C_{LE}) and trailing (C_{TE}) edges, respectively. Behind the spot body is a becalmed region where the turbulence immediately decays and the boundary layer resumes a laminar state.

There are many factors, affecting the characteristics of the turbulent spot and the length of the transition zone, including: the pressure gradient along the streamwise direction, freestream turbulence and surface roughness among others (Mayle, 1991; Jahanmiri, 2011).

Department of Mechanical Engineering, Faculty of Engineering, Kasetsart University, Bangkok 10900, Thailand.
* Corresponding author, e-mail: chaiworw@hotmail.com

Received date : 09/06/14 Accepted date : 24/07/14

However Mayle (1991) stated that the degree of influence of the pressure gradient is much greater than the other factors. As the boundary layer experiences a decelerating flow, it tends to be destabilized. The altered characteristics of the turbulent spot induced by an adverse pressure gradient have been further studied (Gostelow and Dey, 1991; Van Hest *et al.*, 1994; Zhong *et al.*, 2000). Spot celerities at the leading and trailing edges and also the half spreading angle (α) were measured at various pressure gradient parameters. These authors clearly found that when the effect of the adverse pressure gradient is strong, the half spreading angle increases. Nevertheless, only a few contributions (Van Hest *et al.*, 1994; Gostelow *et al*., 1996; Zhong *et al*., 2000) reported on the celerity of the becalmed region (C_{BC}).

A liquid crystal is a substance that is in the phase of a liquid but it is responsible for color-reflecting behavior like a crystal. Over the past few decades, liquid crystals have been used as temperature sensors in a variety of flow visualization applications and Dabiri (2008) described thermochromic liquid crystals (TLCs) with the following relevant details to the current study. TLCs are capable of selectively reflecting wavelengths visible to the human eye as a function of temperature. Generally, a TLC appears as thick milky matter and exhibits coloring birefringence when the temperature reaches its active range. It is usually used as spray to cover a black surface. As the temperature increases, the coated surface turns red, yellow, green and blue. It becomes clear again above the upper limit. It was found that these color changes are reversible and repeatable if the molecules are not physically damaged and chemically degraded. The response time was only 3 ms being short enough for fluid and heat transfer applications (Ireland and Jones, 1987). However, an encapsulated process can strengthen the molecules of a TLC and this process is usually undertaken to avoid physical and chemical degradation. Before use as a temperature indicator, the color play-temperature relation should be defined via a calibration process. The color change properties mainly depend on the prepared composition and the manufacturing process. The selectable range of commercial TLCs is from 30 to 120 °C in a bandwidth of 0.5–20 °C (Dabiri, 2008). Thus, if TLCs are utilized properly, the surface temperature information from over 300,000 points can be provided from the entire surface simultaneously. This amount of data and the excellent spatial resolution are impossible to achieve using any other conventional sensor (Stasiek and Kowalewski, 2002).

In the present study, details of the characteristics of the thermal footprint under the influence of an adverse pressure gradient were further studied using TLCs. The change in the temperature contours underneath the turbulent spot created on the isothermal surface in a low turbulence water tunnel was directly extracted by aid of a developed image processing program. The evolution of the turbulent spot footprint as an instantaneous, spatial distribution of the temperature, convective heat transfer coefficient and heat flux were presented at various pressure gradient parameters. Moreover, the representative structures of the thermal footprint under the pressure gradient were proposed to compare details of the change in spot shape when it was propagated downstream.

EXPERIMENTAL ARRANGEMENT

Experimental setup

The experiment was carried out in low turbulence water tunnel with a section 0.2 m wide by 0.15 m high. It was made from 10 mm Perspex for strength. The early stage of the flow was bled out to refresh a new boundary layer along the leading edge of the flat plate as shown in Figure 1. During the experiment, the aluminum plate was heated by nine strip heaters, closely arranged below the heated plate to create an isothermal surface under the thermal boundary layer. All heaters were discretized for part control using

proportional-integral-derivative (PID) controllers. Local temperature signals were measured from three stations consisting of type-K thin-leaf thermocouples, at 40, 58 and 78 mm from the leading edge. Underneath the heaters, a thermal insulator with high thermal resistance was laid to prevent unwanted power loss. Two rectangular aluminum bars were also assembled below to support both the heaters and the insulator over an air gap as depicted in Figure 2. A black polyvinyl chloride sheet with a thickness of 100 μm was well bonded on the top of the aluminum surface. With its different thermal conductivity, it was found that the plastic sheet plays an important role as a thermal damper. Hence, it was possible to create a continuous, constant, temperature contour on the heated surface.

The spot generator was set up 300 mm downstream from the leading edge. This system was directly controlled by a programmable logic controller board. Instability was induced by injecting water through a 1 mm diameter hole using a solenoid valve. The induced flow was clearly characterized using liquid crystals, coated

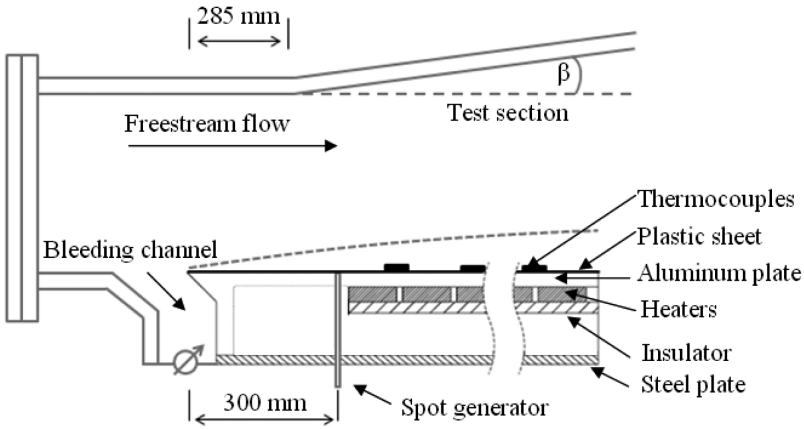

Figure 1 Test section of low turbulence water tunnel.

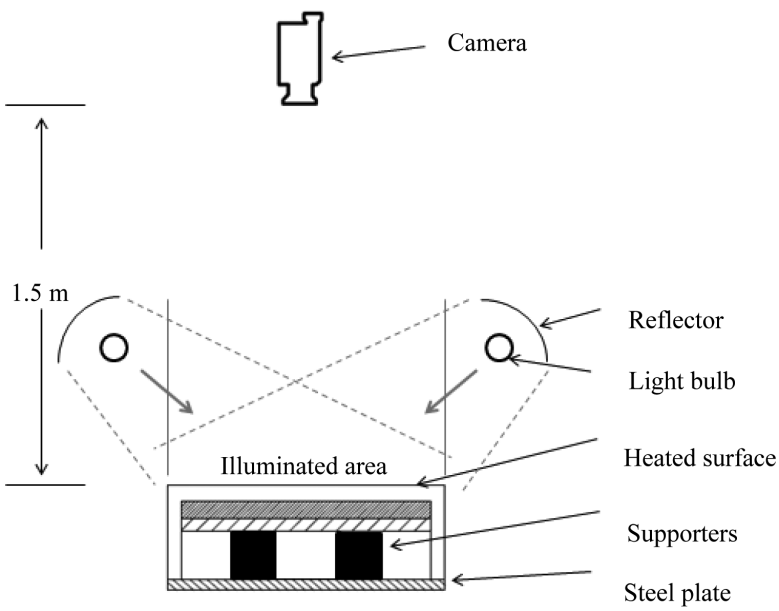

Figure 2 Side view of test section.

about 20 μm thick on top of the plastic sheet. The liquid crystals used were the Chiral Nematic type (Hallcrest; Glenview, IL, USA) and have an active color range of over 2 °C from 27 to 29°C. On top of the LCDs, a clear, continuous overcoat of varnish was sprayed to resist degradation due to the reflective properties of water. Two 70 W fluorescent bulbs with a diameter of 2.54 cm were assembled beside the test section. Their white light, containing all the required spectral wavelengths from red to blue was directed onto the coated plate by glossy reflectors. Image acquisition used a video camera (SDR-H20; Panasonic; Osaka, Japan) with a resolution of 640 × 480 pixels which was installed at an elevation of 1.5 m above the test plate.

Flow conditions

One of the most important parameters that affects the boundary layer transition is the pressure gradient in the streamwise direction. In the present study, it was established by tilting the roof of the test section as shown in Figure 1. The pivot of the tilted roof was at 285 mm downstream from the leading edge of the test plate so the effect of the pressure gradient covered almost the entire test plate including the spot generator. The level of the pressure gradient depended on the elevated angle (β) of the tilted roof. In this study, a mild pressure gradient (MAPG) was set at 2° while the strong level (SAPG) was at 4° from the horizontal. The free stream velocity upstream of the tilting point was kept constant at 0.17 $m.s^{-1}$ throughout the experiment. Downstream of the pivot, the free stream velocity at various points along the plate was measured using a turbine flow meter. The distribution of the free stream velocity under the mild and strong adverse pressure gradients is illustrated in Figure 3.

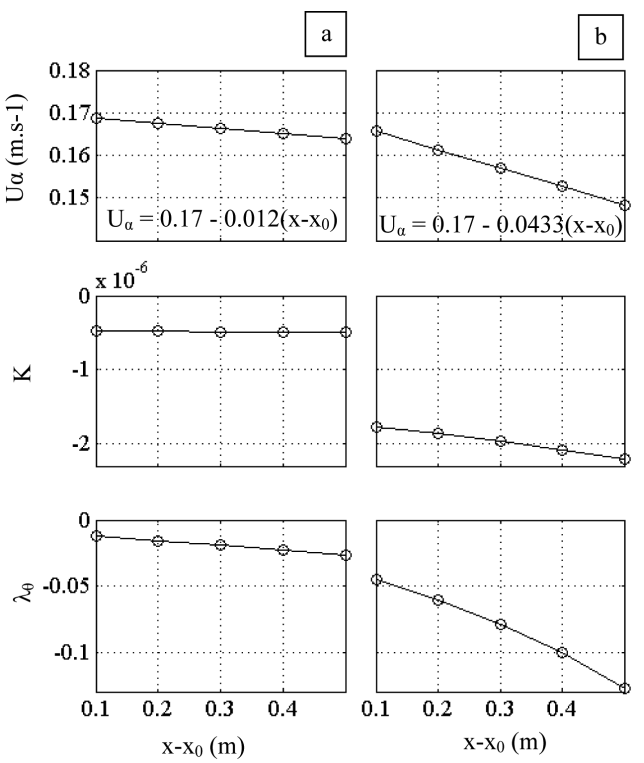

Figure 3 Flow conditions under: (a) Mild pressure gradient and (b) Strong pressure gradient. U_α is the local free stream velocity under the pressure gradient, K is the acceleration parameter and λ_θ is the pressure gradient parameter.

The distribution of the free stream velocity under the pressure gradient as shown in Figure 3a, can be represented by Howarth's profile following Howarth (1938) as Equation 1:

$$U_\alpha = U_0 - a(x - x_0) \quad (1)$$

where U_α is the local free stream velocity under the pressure gradient measured in meters per second, U_0 is the velocity upstream of the pivot measured in meters per second, a is a constant, and x_0 is the distance in meters from the leading edge of the test plate to the tilted point. Figure 3 also shows the distribution of the acceleration parameter (K) and pressure gradient parameter (λ_θ) defined by Thwaites (1987) and shown in Equations 2 and 3, respectively:

$$K = (\upsilon / U_\alpha^2) \cdot (dU_\alpha / dx) \quad (2)$$

$$\lambda_\theta = (\theta^2 / \upsilon) \cdot (dU_\alpha / dx) \quad (3)$$

where υ is the kinetic viscosity, and θ is the laminar boundary layer momentum thickness. θ is calculated from the standard correlations by Thwaites (1987) as shown in Equation 4:

$$\theta^2 = \theta_0^2 + (0.45\upsilon / U_\alpha^6) \int_{x_0}^{x} U_\alpha^5 dx \quad (4)$$

where θ_0 is the momentum thickness at $x = x_0$ and is derived from Equation 5:

$$\theta_0 = 0.671 x_0 / \sqrt{Re_{x_0}} \quad (5)$$

where Re_{x0} is the Reynolds number based on the distance from the leading edge to the tilted point. From Figure 3, it was found that the acceleration parameter and pressure gradient under the strong pressure gradient clearly decreased compared to the mild level. The obtained turbulence intensity (Tu) of the freestream flow was evaluated using Equation 6:

$$Tu = U_{rms} / U_{mean} \quad (6)$$

where U_{rms} is the standard deviation of the velocity and U_{mean} is the mean velocity. The turbulence intensity was 0.925% using a fiber film probe (Dantec Dynamics; Skovlunde, Denmark). Measurements of the velocity profile under unheated laminar boundary layer were conducted at 0.5 m from the leading edge. Although the level of the adverse pressure gradient was increased, the yielded velocity profile still agreed very well with the Blasius profile as shown in Figure 4. At this point, the boundary layer thicknesses were 8.6, 9.4, and 10.6 mm for the zero, mild and strong pressure gradients, respectively. The λ_θ value obtained under the strong pressure gradient was -0.06037. It was more than the critical value of

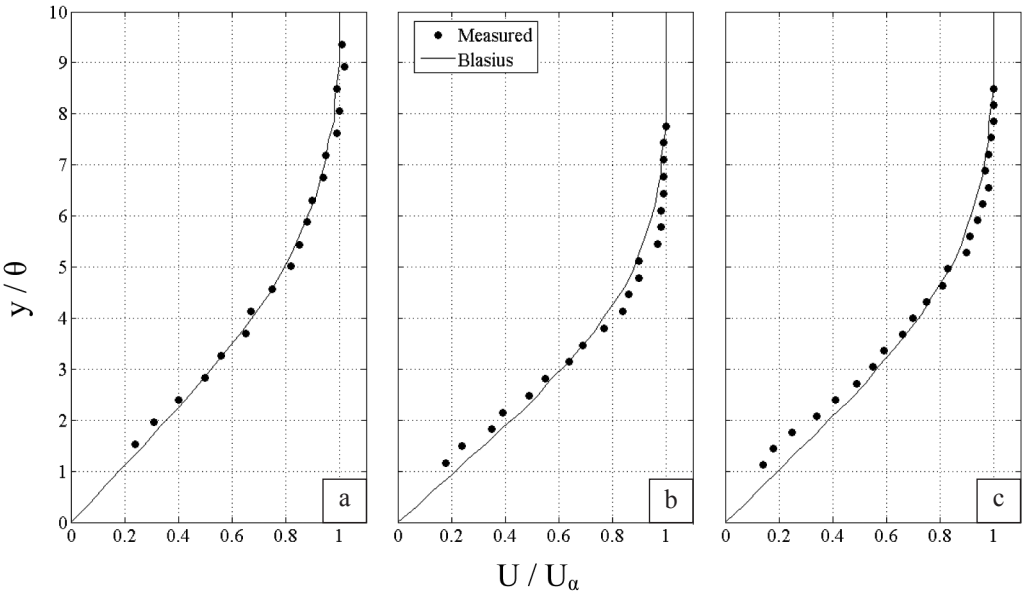

Figure 4 Velocity profiles in the streamwise distance of 0.5 m from leading edge of the heated plate at (a) Zero; (b) Mild; and (c) Strong adverse pressure gradients.

-0.082, which is the verge of separation given by Thwaites (1987).

TECHNICAL ANALYSIS

Image processing and calibration process

The color map of the heated plate generated by the scattering of TLCs was directly recorded in red-green-blue (RGB) format using the video camera. To obtain the distribution of local temperature, an HSI system, (hue, saturation and intensity) was selected as the operating process. In this study, the hue signal, corresponding to a pure color, was used to present the color while saturation and intensity were employed to improve the quality of the obtained results. The relationships between RGB and the HSI format are shown in Equations 7–12 (Russ, 2002):

$$H = \cos^{-1}(Z) \quad \text{if} \quad G \geq R \tag{7}$$

$$H = 2\pi - \cos^{-1}(Z) \quad \text{if} \quad G < R \tag{8}$$

$$Z = (2B - G - R)/(2\cdot\sqrt{(B-G)^2 + (B-R)/(G-R)}) \tag{9}$$

$$I = (R + G + B)/3 \tag{10}$$

$$S = 1 - min(R,G,B)/I \quad \text{if} \quad I > 0 \tag{11}$$

$$S = 0 \quad \text{if} \quad I = 0 \tag{12}$$

where H, S and I are the hue, saturation and intensity signal values, respectively, with a range between 0 and 1 and R, G and B are the color signal values from the RGB color space, respectively. Before the experiment on the transitional flow, the color-temperatures of the TLCs were established using a calibration process. The visible spectrum on the test surface was recorded with a frame rate of 25 frames per second over the elevated temperature, starting from 26.6 up to 28.7 °C in steps of 0.3 °C. When the H signal was extracted from the color at the specified temperature, the accurately calibrated correlation was yielded as Equation 13:

$$T = 58.48270856\cdot H^3 - 61.24566302\cdot H^2 + 23.15642190\cdot H + 23.89758685 \tag{13}$$

This equation was responsible for the transformation from the obtained hue to the local temperature through the experiment. The goodness of fit had a correlation coefficient (R^2) of 0.9987.

Deduction of heat transfer coefficient and heat flux

It is known that the heat flux contours underneath a turbulent spot can represent the shape of the spot footprint, following Kittichaikarn *et al.* (1999). The determination of the local convective heat transfer coefficient is necessary to obtain the heat flux from the principal relationship of heat convection. In the present study, the heat transfer coefficient was numerically achieved by an analytical solution, derived using the implicit energy balance method as Equation 14:

$$\sum_{i=1}^{6} \dot{q}_{(i)\rightarrow(m,n,o)}^{t+\Delta t} = \rho V C_p \frac{T_{m,n,o}^{t+\Delta t} - T_{m,n,o}^{t}}{\Delta t} \tag{14}$$

where $\dot{q}$ is rate of heat transfer, ρ, V, and C_p are the density, controlled volume and specific heat capacity of the plastic sheet, respectively, and Δt is the specified interval time between two consecutive images. The implicit finite difference scheme is found as a backward-difference approximation of the time derivative (Cengel, 2003; Incropera *et al.*, 2007). This scheme provides not only a reduction in the amount of computational time but produces an unconditionally stable state. Unlike the explicit case, this solution needs no restrictions on Δx and Δt. In this study, a control volume of the plastic sheet was established as the interior node m,n,o as shown in Figure 5. The node m,n,o was considered at a time of t and t + Δt, referring to two consecutive frames of the recorded images. The energy exchange in the four lateral nodes was influenced by conduction. The node was subjected to the free stream flow on the upper side. On this side, heat convection occurred and the heat transfer coefficient was evaluated. Finally, the lower side was adjacent to the aluminum plate. It should be noted that this method was performed under the assumption that the temperature at the junction between the plastic sheet and the aluminum plate is constant. The temperature at this point was first determined using Equation 15:

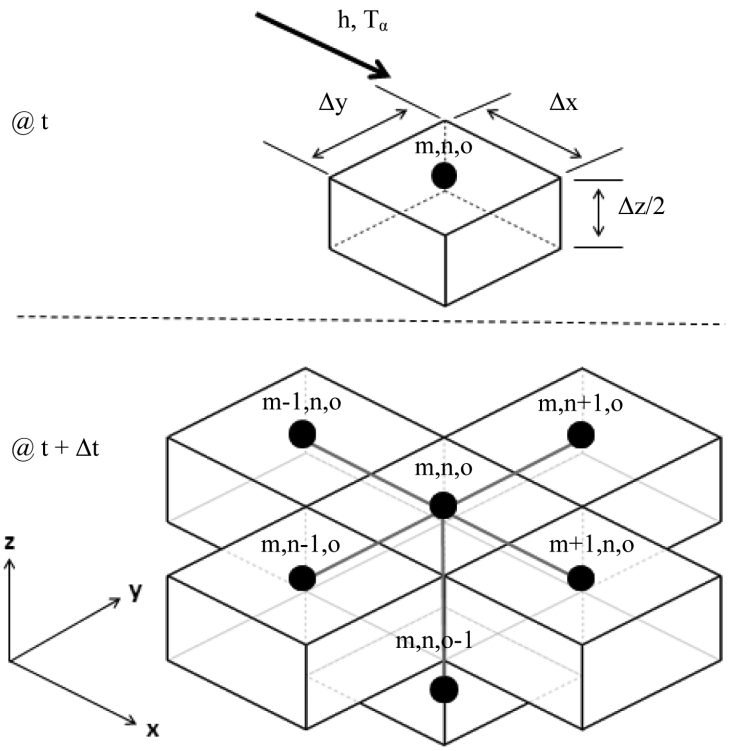

Figure 5 Map of adjoining nodes in an implicit scheme where h is the convective coefficient and T_α is the free stream temperature.

$$T_{m,n,o-1} = \frac{\dot{q} \cdot \Delta z}{k(\Delta x \cdot \Delta y)} + T_{m,n,o} \qquad (15)$$

It should be noted that this method was conducted under the assumption that $T_{m,n,o-1}$ is constant. Thus, in order to find $T_{m,n,o-1}$, $\dot{q}$ could be directly obtained under the condition of laminar flow as in the basic relationship of Equation 16:

$$\dot{q} = h_x(\Delta x \cdot \Delta y)(T_{m,n,o} - T_\alpha) \qquad (16)$$

where h_x is the local heat transfer coefficient. It was obtained from the formulation of the unheated starting length as Equation 17:

$$h_x = \frac{0.332 \cdot Re_x^{1/2} \cdot Pr^{1/3}}{[1-(\xi / x)^{9/10}]^{1/9}} \cdot \frac{k}{x} \qquad (17)$$

where Re_x is the local Reynolds number, Pr is Prandtl's number and ξ is the length of the unheated starting section. Thus, $T_{m,n,o-1}$ would be substituted into Equation 14 to achieve the spatial distribution of the convective heat transfer coefficient and heat flux.

RESULTS AND DISCUSSION

Evolution of thermal footprint of turbulent spot

Each of Figures 6a, 6b and 6c shows the evolution of the thermal footprint of a turbulent spot when it traveled downstream from left to right under a zero, mild and strong pressure gradient, respectively. All images are presented in the RGB colorspace. The selected time interval was set at 0.8 s. The first image was recorded at 1.2 s after disturbance by injecting water. The images were recorded from 0.33 m to 0.6 m from the leading edge of the heated plate in the streamwise direction. On the other axis, zero was set at the midpoint with a span of 0.06 m laterally. Before the spot arrived, the coated liquid crystals were scattered uniformly. The turbulent spot footprint appeared as a patch of a streak. For example, the footprint under a zero pressure gradient is

highlighted inside the oval circle in Figure 6a. It should be noted that all conditions at every level of pressure gradient were set similarly so all results were directly comparable. When the flow was subjected to the increased adverse pressure gradient, it was found that the streaks spread out in a spanwise direction as depicted in by the dotted circles in Figures 6b and 6c.

It should be noted that the camera and the light sources, used during the calibration process and the present experiment were set up under the same conditions. Hence, when the H signal was extracted from the RGB colorspace, the temperature distribution could be precisely obtained by applying the calibrated color-temperature relation as shown in Figures 7a–7c. It was found that the turbulent spot was capable of partly cooling down the heated surface. In this study, the thermal boundary layer generated by the strip heaters started at a distance of 0.33 m. Consequently, the temperatures within the spot footprint in the early stage were relatively low due to the large difference between the temperature of the incoming fluid and the heated surface. However, as the temperatures in each pressure gradient were not outstandingly different, the chilled area increased when the level of the pressure gradient increased. The lowest temperature inside the footprint was measured near the right end of the images. The data trend was similar for the convective heat transfer coefficient, which was determined by employing the analytical solution, developed by the heat balance method mutually with the implicit finite difference approach as shown in Figures 8a–8c. The maximum heat transfer coefficients were found at the core of each streak within the footprint. It was clear that the value of the coefficient inside the induced streaks increased when the level of the pressure gradient was stronger. Therefore, it was found that the pressure gradient along the streamwise distance affected not only the local boundary layer as described previously, but also the heat transfer ability of the turbulent spot.

Structure and parameters of turbulent spot

The shape of the footprint could be directly presented by the distribution of the heat

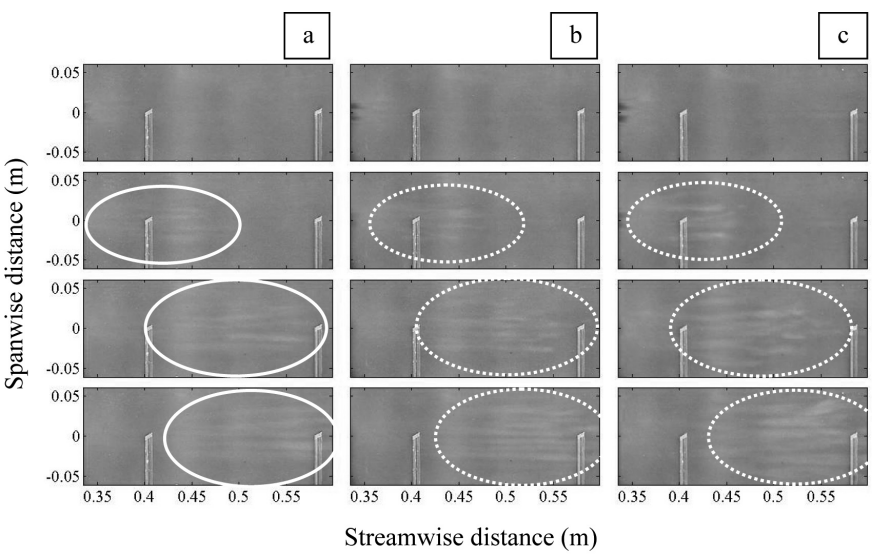

Figure 6 Thermal footprint of turbulent spot under: (a) Zero pressure gradient, where the footprint is highlighted inside the oval circle, (b) Mild pressure gradient and (c) Strong pressure gradient. The white dotted ovals in 6b and 6c show the turbulent spot footprint spreading out in a spanwise direction.

flux beneath the turbulent spot. It was obtained by the principal relationship of heat convection after the local temperature and heat transfer coefficient distributions had been determined. It should be noted that the images obtained from this technique displayed only a part of the turbulent heat flux, acquired from Equation 18:

$$q_{tur} = q_{total} - q_{lam} \quad (18)$$

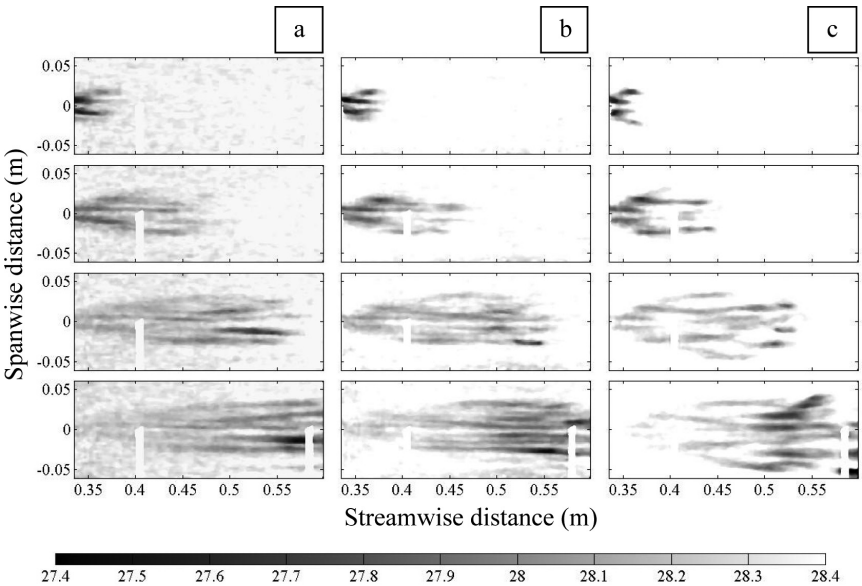

Figure 7 Temperature distribution of thermal footprint under: (a) Zero pressure gradient, (b) Mild pressure gradient and (c) Strong pressure gradient. The horizontal bar at the bottom of the figure shows the calibrated temperature range in degrees Celcius.

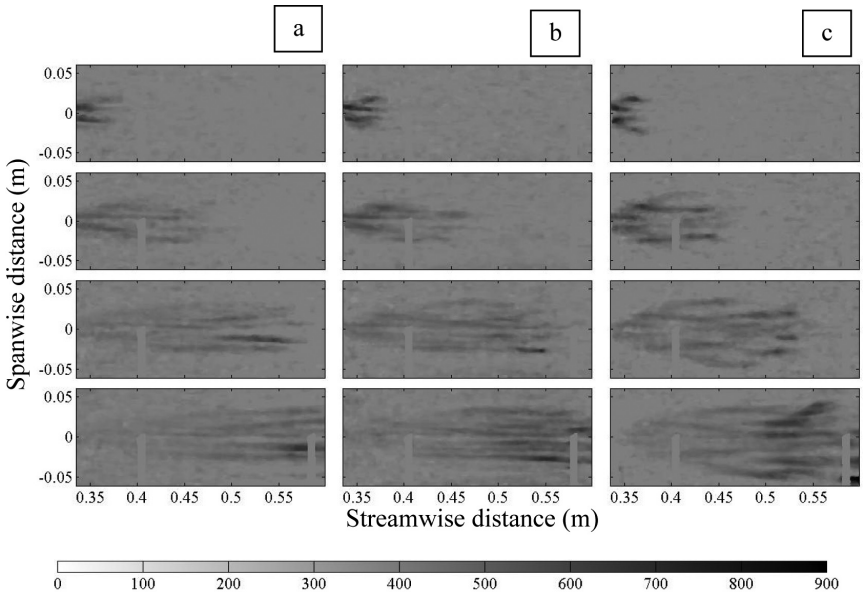

Figure 8 Heat transfer coefficient distribution of thermal footprint under: (a) Zero pressure gradient, (b) Mild pressure gradient and (c) Strong pressure gradient. The bar at the bottom of the figure shows the value of the heat transfer coefficient ($W.m^{-2}.K$).

where q_{total}, q_{tur} and q_{lam} are the total, turbulent and laminar heat flux on the heated surface, respectively. The threshold value for all heat flux contours was set at 10% of $q_{tur,max}$. From the results shown in Figure 9, it was found that the primary structure of the thermal footprint consisted of many streaks inside. When the footprint propagated downstream from left to right, it was found that the pattern of the heat transfer mechanism was similar even as the level of the pressure gradient increased. The footprint started with high heat transfer due to the refreshment of the thermal boundary layer at the left end of the images. It provided a high heat rate again when it convected downstream. It was also clear that not only the size of the footprint but also the maximum heat flux increased under a higher pressure gradient. The structure was more round, which was in agreement with the observations of Gostelow *et al.* (1996). A becalmed region was observed in the trailing area behind the spot body. It appeared as a streaky structure and gradually vanished after the spot had passed.

To eliminate the problem of random effects in the boundary layer transition, a method of establishing the representative structure of the thermal footprint was employed using averaging. This was used to identify the consistent shape of each individual thermal footprint of the artificially generated turbulent spot. This structure was constructed from pixel-by-pixel averaging of the 15 heat flux contours of the footprint. Before processing, the contour was initially non dimensionalized and its bound indicated by the same threshold value as in the heat flux contour. The spatial distribution of the representative structure was obtained from Equation 19:

$$q_{avg} = 1 - \frac{q}{q_{max}} \tag{19}$$

where q_{avg} and q_{max} are the averaged and the maximum heat fluxes, respectively. Figures 10a–10c show the consecutive images of the representative structure of the thermal footprint underneath the turbulent spot under a zero, mild and strong adverse pressure gradient, respectively. These confirm that the size of the footprint increased when the level of the pressure gradient increased. After the disturbance injection, the representative structure contours show that the

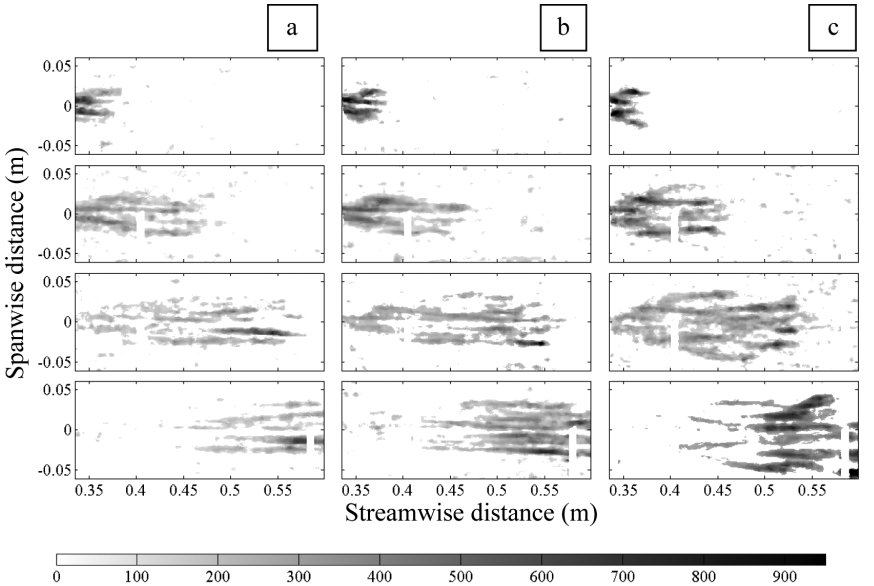

Figure 9 Heat flux distribution of thermal footprint under: (a) Zero pressure gradient, (b) Mild pressure gradient and (c) Strong pressure gradient. The bar at the bottom of the figure shows the value of the heat flux ($W.m^{-2}$).

near wall turbulence within the turbulent spot broke down into four frontal streaks. A similar behavior was found in all pressure gradients. Fifth and sixth streaks, induced by the new subsidiary vortex, were described by Haidari and Smith (1994), and can be seen near both wingtips as shown in Figure 10b. These additional streaks occurred more quickly if the pressure gradient was stronger. The shape of the becalmed region in the representative structure was first visible as a long tail. Later, it gradually decayed into two tail-like structures. In addition, the end point of this region was used to define spot celerity in the becalmed region as shown in Table 1.

When the turbulent spot was under the influence of an adverse pressure gradient, spot celerities could be directly obtained from the particular velocity of the footprint over the constant freestream velocity of water. It should be noted that under an adverse pressure gradient, the freestream velocity decreased in the streamwise direction. If the celerity was assumed to be constant through the two successive points on the surface, the algorithm was altered to Equation 20:

$$C = \frac{1}{\Delta t} \int_{x1}^{x2} \frac{dx}{U_{\alpha}(x)} \tag{20}$$

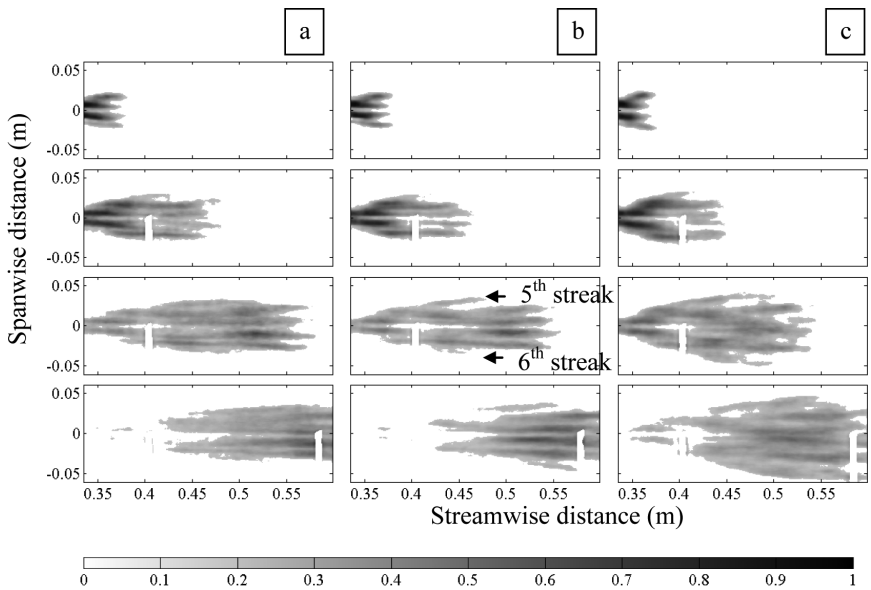

Figure 10 Representative structure of thermal footprint under: (a) Zero pressure gradient, (b) Mild pressure gradient and (c) Strong pressure gradient. The horizontal bar at the bottom of the figure shows non-dimensional heat flux, defined in Equation 19.

Table 1 Turbulent spot parameters under adverse pressure gradient.

Study	λ_θ	C_{LE}	C_{TE}	C_{BC}	α(°)
Zhong *et al.* (2000)	-0.08	0.74	0.42	0.22	13
Present study (SAPG)	-0.06	0.65±0.03	0.44±0.02	0.22±0.01	11.4±0.02
Gostelow *et al.*(1996)	-0.057	0.872	0.431	0.25	29.2
Van Hest (1994)	-0.036	0.92	0.38	0.1	17
Zhong *et al.* (2000)	-0.03	0.78	0.49	0.27	9
Present study (MAPG)	-0.016	0.71±0.03	0.49±0.02	0.28±0.01	8.9±0.02

SAPG = Strong adverse pressure gradient; MAPG = Mild adverse pressure gradient; λ_θ = Pressure gradient parameter; C_{LE} = Leading edge celerity; C_{TE} = Trailing edge celerity; C_{BC} = Becalmed region celerity; α = Half spreading angle.

where C is the spot celerity, Δt is the interval time between two successive distance of x1 and x2 and $U_\alpha(x)$ is freestream velocity function as shown in Figure 3. Details of the measurement technique in this study were reported by Zhong *et al.* (2000). The uncertainties were also determined following Weerachai (2014). The present study provided celerities of the footprint under a mild pressure gradient of 0.71 ± 0.03, 0.49 ± 0.02 and 0.28 ± 0.01 at the leading edge, trailing edge and the end point of the becalmed region, respectively. They became 0.65 ± 0.03, 0.44 ± 0.02 and 0.22 ± 0.01 under the strong pressure gradient. It was found that, unlike the half spreading angle, the value of celerities tended to decrease when λ_θ decreased. The half spreading angles were 8.9 ± 0.02 and 11.4 ± 0.02 ° when the footprint experienced the mild and strong pressure gradients, respectively. From Table 1, it should be noted that it was only in the results from Zhong *et al.* (2000) that turbulent spot parameters were measured on the exact surface. Consequently, not only the celerity at the leading edge but also the half spreading angle were relatively higher in Gostelow *et al.* (1996) and Van Hest *et al.* (1994). It was found that their high celerities were measured on elevated locations. This caused the apparently higher value because this location had relatively less shear force generated by the viscous boundary layer. This phenomenon was also found in the appearance of the velocity profile under the boundary layer and it strongly affected the propagation rate of the turbulent spot at the leading edge. In addition, the higher half spreading angle resulted from the presence of the wave packet, measured by Gostelow *et al.* (1996). However, the spot parameters obtained in the current study were in agreement with those reported by Zhong *et al.* (2000). The location of the virtual onset of the turbulent spot under the adverse pressure gradient could be depicted as shown in Figure 11. It was found that the virtual onset achieved relied on being located at 0.167, 0.222 and 0.267 m from the leading edge when the pressure gradient was increased. Thus, this confirmed that the length of the transition zone could be directly controlled by the influence of the pressure gradient.

CONCLUSION

Experimental investigation was undertaken on the thermal footprint of an artificially created turbulent spot under a zero, mild and strong pressure gradient. Evolution of the footprint was visualized using coated liquid crystals mutually with the developed image processing program. The implicit finite element method was derived in the energy balance scheme to deduce the distribution of the heat transfer coefficient and heat flux. From the results, it was found that the change in the pressure gradient directly affected the thermal behavior of the footprint. Not only the heat rate, but also the heat exchange area increased when the level of pressure gradient was stronger. The proposed representative structure showed that the footprint underneath the turbulent spot appeared as four frontal streaks in the early stage. Two additional streaks occurred at its lateral bound when the spot propagated further downstream. The spot parameters obtained were in agreement with those reported by other researchers. Thus, these results were capable of providing information from qualitative and quantitative data using numerically predictive formulas to determine the flow under boundary layer transition induced by an adverse

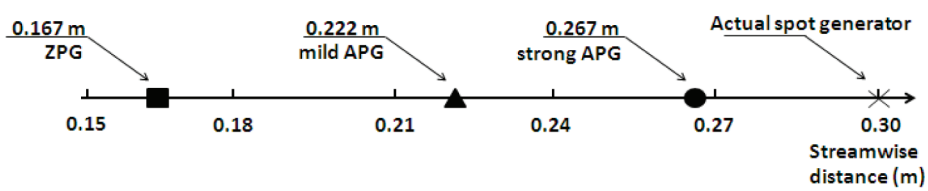

Figure 11 Location of virtual onset of turbulent spot footprint under various adverse pressure gradients.

pressure gradient.

ACKNOWLEDGEMENT

The authors gratefully acknowledge the financial support of the Kasetsart University Research and Development Institute (KURDI).

LITERATURE CITED

Cengel, Y.A. 2003. **Heat Transfer: A Practical Approach.** 2nd ed. McGraw-Hill. New York, NY, USA. 932 pp.

Dabiri, D. 2008. Digital particle image thermometry/velocimetry: a review. **Exp. Fluids.** 46(2):191–241.

Emmons, H.W. 1951. The laminar-turbulent transition in a boundary layer-part I. **J. Aerosp. Sci.** 18: 490–498.

Gostelow, J.P. and A.R. Dey. 1991. Spot formation rates in transitional boundary layers under zero and adverse pressure gradients. *In* **Proceedings of Conference in Boundary Layers Transition and Control,** 8-12 April 1991. Cambridge, UK.

Gostelow J.P., N. Melwani and G.J. Walker. 1996. Effects of streamwise pressure gradient on turbulent spot development. **J. Turbomach.** 118: 737–743.

Haidari, A.H. and C.R. Smith. 1994. The generation and regeneration of single hairpin vortices. **J. Fluid Mech.** 277: 135–162.

Howarth, L. 1938. On the solution of the laminar boundary layer equations. *In* **Proceedings of the Royal Society of London series A.** 18 February 1938. London, UK.

Incropera, F.P., D.P. Dewitt, T.L. Bergman and A.S. Lavine. 2007. **Fundamentals of Heat and Mass Transfer.** 6th ed. John Wiley & Sons. Hoboken, NJ, USA. 925 pp.

Ireland, P.T. and T.V. Jones. 1987. The response time of a surface thermometer employing encapsulated thermochromic liquid crystals. **J Phys. E: Sci. Instrum.** 20: 1195–1199.

Jahanmiri, M. 2011. **Boundary Layer Transitional Flow in Gas Turbines.** Research report: 01 ISSN 1652-8549. Göteborg, Sweden. 51 pp.

Kittichaikarn, C., P.T. Ireland, S. Zhong and H.P. Hodson. 1999. An investigation on the onset of wake-induced transition and turbulent spot production rate using thermochromic liquid crystal. *In* **Proceedings of 44th ASME International Gas Turbine and Aeroengine Congress and Exposition,** 7–10 June 1999. Indianapolis, IN, USA.

Mayle, R.E. 1991. The role of laminar-turbulent transition in gas turbine engine. **Trans. J. Turbomach.** 113: 509–537.

Russ, J.C. 2002. **The Image Processing Handbook.** 6th ed. CRC Press. Boca Raton, FL, USA 885 pp.

Schubauer, G.B. and P.S. Klebanoff. 1955. **Contribution on the Mechanism of Boundary Layer Transition.** National Advisory Committee for Aeronautics Technical Note 3489. Washington, DC, USA. 31 pp.

Stasiek J.A. and T.A. Kowalewski. 2002. Thermochromic liquid crystals applied for heat transfer research. **Opto-Electron. Rev.** 10(1): 1–10.

Thwaites, B. 1987. **Incompressible Aerodynamics.** Dover Publications. NY, USA. 636 pp.

Van Hest, B.F.A., D.M. Pesschier and J.L. Van Ingen. 1994. The development of a turbulent spot in an adverse pressure gradient boundary layer. *In* **Proceedings of IUTAM Symposium,** 5-9 September 1994. Sendai, Japan.

Walker, G.J. and J.P. Gostelow. 1998. Comparison between triggered turbulent spots and wake-induced turbulent patches on compressor blading. *In* **Proceeding of 13th Australasian Fluid Mechanics Conference,** 13-18 December 1998. Melbourne, VIC, Australia.

Weerachai, C. 2014. **Investigation of 3D Structure of Turbulent Spot using Liquid Crystals.** D. Eng. Thesis, Kasetsart University. Bangkok, Thailand. 177 pp.

Zhong, S., C. Kittichaikarn, H.P. Hodson and P.T. Ireland. 2000. Visualisation of turbulent spots under the influence of adverse pressure gradients. **Exp. Fluids** 28: 385–393.